

Neural Power-Optimal Magnetorquer Solution for Multi-Agent Formation and Attitude Control

Yuta Takahashi^{1,2} Shin-ichiro Sakai³

Abstract—This paper presents a learning-based current calculation model to achieve power-optimal magnetic-field interaction for multi-agent formation and attitude control. In aerospace engineering, electromagnetic coils are referred to as magnetorquer (MTQ) coils and used as satellite attitude actuators in Earth’s orbit and for long-term formation and attitude control. This study derives a unique, continuous, and power-optimal current solution via sequential convex programming and approximates it using a multilayer perceptron model. The effectiveness of our strategy was demonstrated through numerical simulations and experimental trials on the formation and attitude control.

Index Terms—Multi-Robot Systems, Model Learning for Control, Space Robotics and Automation

I. INTRODUCTION

THE magnetic field provides a sophisticated control system used in medicine, biomimetic robotics, and the aerospace field. Typically, they are generated by coils that wind conductive wires around magnetic materials or an air core. The current passing through these conductors generates a magnetic field. Its interaction with the surrounding magnets provides relative position and orientation information while generating electromagnetic forces and torques. In the medical field, magnetic resonance imaging is a well-known technique that uses magnetic fields to produce non-invasive images of internal structures. In biomedical robotics, these fields have been employed to steer miniature robots inside the human body, enabling targeted drug delivery and minimally invasive procedures [1]. The aerospace community originally utilized this actuation in the geomagnetic field as a satellite attitude actuator [2] and applied satellite state estimation [3].

Multi-agent control methodologies using magnetorquers (MTQs) have been developed for the aerospace community. They use magnetic interactions to control the formation and attitudes of satellites. This actuation originally have underactuation for six degrees-of-freedom (DoF) control for N systems [4], [5]. To deal this, previous work considered time-integrated current control to extend the controllability for 6-DoF swarm control. Their examples include a time-scheduled switching topology [6] and alternating current (AC) modulation [4], which controls the amplitude and phase of the AC. The advantage of AC modulation also lies in the decoupling of magnetic interactions from different frequencies, including a geomagnetic field that enables decentralized control [5].

¹Graduate Student, Department of Mechanical Engineering, Tokyo Institute of Technology, Ookayama Meguro, Tokyo 152-8552, Japan, takahashi.y.cl@m.titech.ac.jp

²Researcher, Satellite Research and Development, Interstellar Technologies Inc., 149-7 Hiroo, Hokkaido 089-2113, Japan

³Professor, Department of Spacecraft Engineering, Japan Aerospace Exploration Agency,3-1-1 Yoshinodai, Sagami-hara, Kanagawa 252-5210, Japan

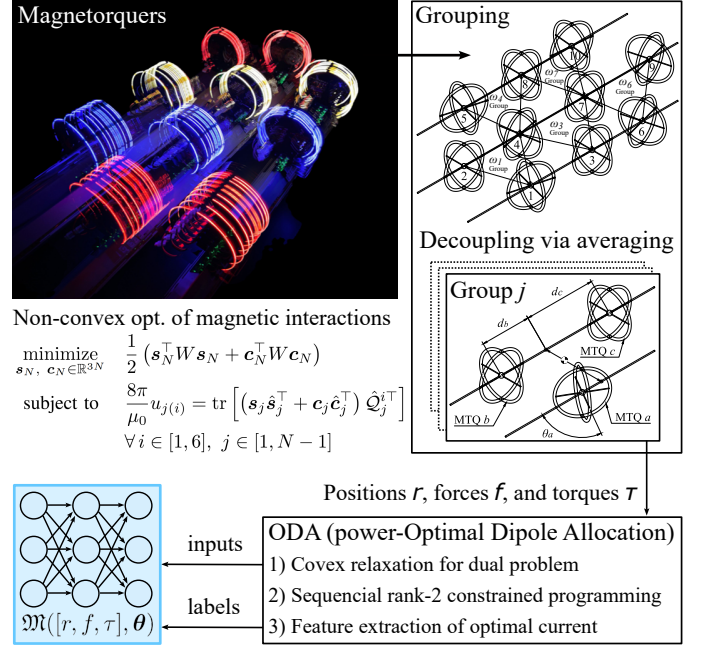


Fig. 1. Offline supervised learning of power-optimal dipole allocation model NODA for magnetically actuated multi-agent control.

This actuation provides promising applications for proximity operations [7] and large distributed space structures [8], [9].

Their drawback is that the solution of a computationally intensive optimization problem is required to derive the currents for coordinated magnetic-field interaction, which we refer to as “dipole allocation.” This problem contains inherent non-convex constraints [4], rendering it an NP-hard non-convex quadratically constrained quadratic program (QCQP). As the problem dimensions increase, finding the global optimal solution becomes computationally expensive. Prior studies have explored several computational strategies. General optimization techniques have been applied to derive all optimal solutions [10] or track a viable solution using the solution from a previous step [4], [11]. The closed-form Jacobian and Hessian expressions support efficient calculations as specialized methods for this system [12]. For the two-satellite force control case, a unique global minimum power solution was analytically derived in a closed form [13]. However, space-qualified processors offer limited computational capabilities, rendering global solvers impractical. Local solvers provide no performance guarantees, and these locally optimal dipole moment solutions can be discontinuous because the solvers can jump between distinct local minima [4]. This can result in impulsive input and high-frequency disturbances. More-

over, recent applications [8], [9] assume simultaneous high-precision control of both the position and attitude without additional actuators and require repeated current computation. These require the optimal dipole solutions to be computed using a significantly reduced computational burden.

To this end, we derive a learning-based approximation algorithm called Neural power-Optimal Dipole Allocation (NODA) for real-time optimal dipole allocation. We also present a systematic multileader-based decentralized control strategy to improve scalability and reduce the sample region. The remainder of this paper is organized as follows: Section II introduces the MTQ system for 6DoF swarm control. Section III derives a systematic decoupling approach focusing on a small group. In Section IV, we formulate the optimal dipole allocation problem with a proof of its control-induced disturbance reduction and baseline allocation. Section V presents our main results, a continuous, optimal dipole solution derived by ODA that can be approximated by a multilayer perceptron (MLP) model using NODA. Numerical and experimental evaluations validate the effectiveness of the proposed methods and trained model in Section VI and Section VII concludes paper.

II. PRELIMINARIES

A. Magnetic Interaction Approximation Model

We first introduces the dipole approximation of the magnetic field $B_k(\mu_k, r_{jk})$, “far-field” model [10]. We denote the j th magnetic moment as $\mu_j = N_t A c (1 + \gamma) \mathbf{n}$ where N_t is the number of coil turns, c is the current strength, A is the area enclosed by the coil, $\mathbf{n} \in \mathbb{R}^3$ is the unit vector perpendicular to the coil plane, and γ is the iron-core ratio [5]. This derives force $f_{j \leftarrow k}(\mu_j, r_{j \leftarrow k}) = \nabla(\mu_j \cdot B_k)$ and torque $\tau_{j \leftarrow k}(\mu_j, r_{j \leftarrow k})$ exerted on the j th agent by the k th one:

$$f_{j \leftarrow k} = \frac{3\mu_0/4\pi}{d_{j \leftarrow k}^4} \left[\frac{\mu_k \cdot \mu_j - 5M_k M_j}{d_{j \leftarrow k}} r_{j \leftarrow k} + M_k \mu_j + M_j \mu_k \right]$$

$$\tau_{j \leftarrow k} = \mu_j \times B_k = \frac{\mu_0/4\pi}{d_{j \leftarrow k}^3} \mu_j \times \left[\frac{3M_k}{d_{j \leftarrow k}} r_{j \leftarrow k} - \mu_k \right],$$

where $M_k = \frac{\mu_k \cdot r_{j \leftarrow k}}{d_{j \leftarrow k}}$ and $d_{j \leftarrow k} = \|r_{j \leftarrow k}\|$. We can also use exact model [10] or its learning-based approximation [7], [14].

B. Time-Integrated 6-DoF MTQ Control

We introduce the AC modulation for 6-DoF control. Let us assume the j th agent drives sinusoidal currents as follows:

$$\mu_j(t) = \mu_j^{\text{amp}} \sin(\omega_j t + \psi_j) = s_j \sin(\omega_j t) + c_j \cos(\omega_j t), \quad (1)$$

where the amplitudes $\mu_{j,k}^{\text{amp}} \in \mathbb{R}^3$, angular frequency $\omega_j \in \mathbb{R}$, phase $\theta \in \mathbb{R}^3$, and sine and cosine amplitudes $s_j, c_j \in \mathbb{R}^3$. We define the first-order averaged input from the neighbor as $u_{j \leftarrow k}^{\text{avg}} \triangleq \sum_{k \neq j} u_{j \leftarrow k}^{\text{avg}}$, where $u_{j \leftarrow k}^{\text{avg}} = [f_{j \leftarrow k}^{\text{avg}}; \tau_{j \leftarrow k}^{\text{avg}}]$:

$$u_{j \leftarrow k}^{\text{avg}} \triangleq \int_T \sum_{k \neq j} \left[\begin{array}{l} f_{j \leftarrow k}(\mu_k(\tau), \mu_j(\tau), r_{jk}) \\ \tau_{j \leftarrow k}(\mu_k(\tau), \mu_j(\tau), r_{jk}) \end{array} \right] \frac{d\tau}{T}$$

$$= \frac{1}{2} \left[\begin{array}{l} f_{j \leftarrow k}(s_{j,k}, r_{j \leftarrow k}) + f_{j \leftarrow k}(c_{j,k}, r_{j \leftarrow k}) \\ \tau_{j \leftarrow k}(s_{j,k}, r_{j \leftarrow k}) + \tau_{j \leftarrow k}(c_{j,k}, r_{j \leftarrow k}) \end{array} \right] \quad (2)$$

where we use the fact that the agent does not interact with other frequency effects in the first-order averaged dynamics

[4], i.e., $\int u_{j \leftarrow k} dt \approx 0$ for $\omega_k \neq \omega_j$. This modulation increases the number of variables and extends the controllability to realize 6-DoF control for an arbitrary number of agents [4]. We assume all n agents have a circular triaxial MTQ and $m \in [1, n]$ agents are equipped with 3-axis RWs. As its control does not change the angular momentum $\sum_{j=1}^n (m_j r_j \times \dot{r}_j + I_j \cdot \omega_j) + \sum_{j=1}^m h_j = L \Leftrightarrow$

$$A_{(n,m)} \zeta \triangleq \begin{bmatrix} m_1 [r_1^i]_{\times}, \dots, m_n [r_n^i]_{\times}, \\ C^{I/B_1} J_1, \dots, C^{I/B_n} J_n, \\ C^{I/B_1}, \dots, C^{I/B_m} \end{bmatrix} \begin{bmatrix} \dot{r}^a \\ \omega^b \\ \xi^b \end{bmatrix} = 0, \quad (3)$$

where $A_{(n,m)} \in \mathbb{R}^{3 \times (6n+3m)}$ and the states are $\zeta \in \mathbb{R}^{6n+3m}$. A previous study-derived commands $u_c \in \mathbb{R}^{6n+3m}$ for the submanifold stabilization of magnetically actuated swarms [4].

Theorem II.1 (Kinematics Control [4]). *Let $S_{(n,m)}$ be the tangent space of angular momentum conservation $S_{(n,m)}$, e.g.,*

$$S_{(n,m)} = \left[\begin{array}{c} E_{(21)} \\ -C^{B_2/I} A_{(n,m)}[:, 1:\text{end}-3] \end{array} \right] \in \text{Null Space}(A_{(n,m)})$$

Then, the magnetic interaction can realize $u_c = [f_c^a; \tau_c^b; \dot{h}_c^b] = B_{(n,m)}^{-1} M_{(n,m)} S_{(n,m)} u_c$ where the arbitrary auxiliary commands are $u_c \in \mathbb{R}^{6n+3m-3}$, the inertia matrix is $M_{(n,m)}$, and the input matrix is $B_{(n,m)} \in \mathbb{R}^{(6n+3m) \times (6n+3m)}$ in [4].

III. MULTILEADER-BASED DECENTRALIZED CONTROL

This section presents a multileader-based dipole allocation that decentralizes large-scale agent systems into smaller groups. We define n agent nodes as $\mathcal{V} = \{1, \dots, n\}$ and the edge set as $\mathcal{E} \subseteq \mathcal{V} \times \mathcal{V}$, where edge $(j, k) \in \mathcal{E}$ denotes that the k th node obtain some information from the j th node.

We define a directed multileader graph $\mathcal{G}^{\text{ml}}(\mathcal{V}, \mathcal{E}^{\text{ml}} = \bigcap_j \mathcal{E}_j^{\text{ml}})$ and assign specific agents to the leader subset $\mathcal{V}_l \in \mathcal{V}$ with a unique frequency $\omega_{k \in \mathcal{V}_l}$. Its edges $(j, k) \in \mathcal{E}_j^{\text{ml}}$ describe the hierarchical relationships of $j \in \mathcal{V}_l$ and $k \in \mathcal{V}$, i.e., the k th agents drive the $\omega_{j \in \mathcal{V}_l}$ current. This extends the dipole moment in (1) into the multi-frequency one:

$$\mu_k(t) = \sum_{j \in \mathcal{V}_l} (s_{k[j]} \sin(\omega_j t) + c_{k[j]} \cos(\omega_j t)), \quad (4)$$

where $s_{k[j]}, c_{k[j]} \in \mathbb{R}^3$ is the k th sine and cosine amplitude in the $j \in \mathcal{V}_l$ th leader group. One cycle T and each ω_j should be derived to cancel out the coupling between different frequencies and hold the first-order approximation in (2) as follows:

$$\forall 1 \leq i < j \leq n, \quad T \triangleq \frac{\text{lcm} \left(\frac{2\pi k_{\text{int}}}{2\omega_i}, \frac{2\pi k_{\text{int}}}{|\omega_i - \omega_j|}, \frac{2\pi k_{\text{int}}}{\omega_i + \omega_j} \right)}{k_{\text{int}}} \quad (5)$$

where $\text{lcm}(\cdot)$ is the least common multiple and the coefficient k_{int} ensures the elements of $\text{lcm}(\cdot)$ are integers. For a user-defined T_{max} , the necessary conditions for $T \leq T_{\text{max}}$ are

$$\omega_i \geq \frac{\pi}{T_{\text{max}}}, \quad |\omega_i - \omega_j| \geq \frac{2\pi}{T_{\text{max}}}, \quad \omega_i + \omega_j \geq \frac{2\pi}{T_{\text{max}}},$$

such that the elements in (5) satisfy $T \leq T_{\text{max}}$.

Remark 1. *One easy way to select ω_i for a given T_{max} is*

$$\omega_i = \frac{2\pi i}{T_{\text{max}}} \quad \text{s.t.} \quad T = \frac{\text{lcm} \left(\frac{k_{\text{int}}}{2i}, \frac{k_{\text{int}}}{|i-j|}, \frac{k_{\text{int}}}{i+j} \right)}{k_{\text{int}}/T_{\text{max}}} = T_{\text{max}}.$$

IV. PROBLEM FORMULATION OF THE POWER-OPTIMAL DIPOLE ALLOCATION WITH BASELINE ALLOCATION

This section formulates the power-optimal dipole allocation problem and the baseline non-optimal one in Algorithm 1.

A. Baseline: Decentralized Dipole Allocation

Motivated by prior work [13], we derive the baseline decentralized dipole allocation using an inverse matrix. First, we simplify the time-averaged far-field magnetic interaction model as a bilinear polynomial formulation. For given the arbitrary vectors $v^a, w^a \in \mathbb{R}^3$, we newly define the coordinates such that its x -axis aligns with v^a , i.e., $\mathbf{e}_x = \text{nor}(v^a)$, its y -axis is orthogonal to v^a , and w^a satisfies $\mathbf{e}_y = \text{nor}(S(v^a)w^a)$. This yields the following coordinate transformation matrix:

$$\mathcal{C}(v^a, w^a) = \left[\mathbf{e}_x = \frac{v^a}{\|v^a\|}, \mathbf{e}_y = \frac{[v^a]_{\times} w^a}{\|[v^a]_{\times} w^a\|}, \mathbf{e}_z = \mathbf{e}_x \times \mathbf{e}_y \right]. \quad (6)$$

Definition 1. The line-of-sight frame $\{\mathcal{LOS}_{j \leftarrow k}\}$, fixed for the k th agent so that it can see the j th one, is defined by (6) such that its coordinate transformation matrix $C^{O/L_{j \leftarrow k}} \in \mathbb{R}^{3 \times 3}$ is

$$C^{A/L_{j \leftarrow k}} = \mathcal{C}(r_{j \leftarrow k}^a, S(f_j^a)r_{j \leftarrow k}^a), \quad (7)$$

where x -axis in \mathcal{LOS} is aligned with r_{jk} and f_j remains in the x - y plane in \mathcal{LOS} , i.e., $r_{j \leftarrow k}^{l_{j \leftarrow k}} = [\|r_{j \leftarrow k}^a\|; 0; 0]$ and $f_j^{l_{j \leftarrow k}} = 0$.

The frame in Definition 1 yields the bilinear polynomial formulation in (2) with the constant matrix

$$u_{j \leftarrow k}^a = \frac{1}{2} \frac{\mu_0}{4\pi} Q_{j \leftarrow k} (s_k^a \otimes s_j^a + c_k^a \otimes c_j^a), \quad (8)$$

where $d_{j \leftarrow k} = \|r_{j \leftarrow k}\|$ and $Q_{j \leftarrow k} \in \mathbb{R}^{6 \times 9}$ is

$$Q_{j \leftarrow k} = (I_2 \otimes C^{A/L_{j \leftarrow k}}) \begin{bmatrix} \Psi_f(d_{j \leftarrow k}) \\ \Psi_\tau(d_{j \leftarrow k}) \end{bmatrix} (C^{L_{j \leftarrow k}/A} \otimes C^{L_{j \leftarrow k}/A})$$

$$\begin{cases} \Psi_f(d_{j \leftarrow k}) = \frac{1}{d_{j \leftarrow k}^4} \begin{bmatrix} -6 & 0 & 0 & 0 & 3 & 0 & 0 & 0 & 3 \\ 0 & 3 & 0 & 3 & 0 & 0 & 0 & 0 & 0 \\ 0 & 0 & 3 & 0 & 0 & 0 & 3 & 0 & 0 \end{bmatrix} \\ \Psi_\tau(d_{j \leftarrow k}) = \frac{1}{d_{j \leftarrow k}^3} \begin{bmatrix} 0 & 0 & 0 & 0 & 0 & 1 & 0 & -1 & 0 \\ 0 & 0 & 2 & 0 & 0 & 0 & 1 & 0 & 0 \\ 0 & -2 & 0 & -1 & 0 & 0 & 0 & 0 & 0 \end{bmatrix} \end{cases}$$

where $\sigma_{\max}(\Psi_f) = \sqrt{54}/d_{j \leftarrow k}^4$ and $\sigma_{\max}(\Psi_\tau) = \sqrt{5}/d_{j \leftarrow k}^3$. We allocate a dipole for two agents in a decentralized manner. In (8), we randomly predetermine one dipole as a constant indexed by 0, e.g., $\{s_{F0}, c_{F0} \in \mathbb{R}^3 \mid \|s_{F0}\| = \|c_{F0}\| = 1\}$. This derives another one using the inverse matrix calculation

$$\begin{cases} \begin{bmatrix} s_L^{los} \\ c_L^{los} \end{bmatrix} = \left\{ \frac{\mu_0}{8\pi} Q_{L \leftarrow F} \left([s_{F0}^{los}, c_{F0}^{los}] \otimes E_3 \right) \right\}^{-1} u_{L \leftarrow F}^{los} \\ \begin{bmatrix} s_F^{los} \\ c_F^{los} \end{bmatrix} = \left\{ \frac{\mu_0}{8\pi} Q_{L \leftarrow F} \left(E_3 \otimes [s_{L0}^{los}, c_{L0}^{los}] \right) \right\}^{-1} u_{L \leftarrow F}^{los} \end{cases} \quad (9)$$

We make their norms uniform to minimize $\|\mu_N^{\text{amp}}\|^2$:

$$\{s_L, c_L\} = \frac{\{s_{L0}, c_{L0}\}}{\sqrt{\|\{s_{L0}, c_{L0}\}\|}}, \quad \{s_F, c_F\} = \frac{\{s_{F0}, c_{F0}\}}{1/\sqrt{\|\{s_{L0}, c_{L0}\}\|}}.$$

Remark 2. We note the necessary conditions for the existence of the inverse in (9). Without loss of generality, we can set $\theta_{j(1)}^{los} = 0$ as $s_{F0} = [\mu_{F(1)}^{\text{amp}}; \mu_{F(2)}^{\text{amp}} \cos \theta_{F(2)}; \mu_{F(3)}^{\text{amp}} \cos \theta_{F(3)}]$

Algorithm 1 Inverse-based dipole allocation based on (9).

- 1: **Inputs:** trial number n_{rand} , $r_{L \leftarrow F} \in \mathbb{R}^3$, $u_{L \leftarrow F}^{los} \in \mathbb{R}^6$
- 2: **Outputs:** $[s_L; s_F; c_L; c_F]^{(i^*)} \in \mathbb{R}^{12}$, $W_{\text{power}} \in \mathbb{R}$
- 3: **for** $i \in [1, n_{\text{rand}}]$ **do**
- 4: Derive randomly $[s_L; s_F; c_L; c_F]^{(i)}$ by (9) and $W_{\text{power}}^{(i)}$
- 5: **end for**
- 6: Choose $[s_L; s_F; c_L; c_F]^{(i^*)}$ satisfies $i^* = \arg \min W_{\text{power}}^{(i)}$

and $c_{F0} = [0; \mu_{F(2)}^{\text{amp}} \sin \theta_{F(2)}; \mu_{F(3)}^{\text{amp}} \sin \theta_{F(3)}]$ where $\{\text{los}\}$ are dropped in the remainder. A symbolic calculation verifies that $\mu_{F(1)}^{\text{amp}} \mu_{F(2)}^{\text{amp}} \mu_{F(3)}^{\text{amp}} \sin(\theta_{F(2)} - \theta_{F(3)}) \neq 0$ guarantees the existence of an inverse. Its orthogonal vector $\mu_{F0\perp}$ satisfies

$$\mu_{F0\perp} // (c_{F0} \times s_{F0}) = \begin{bmatrix} \mu_{j(2)}^{\text{amp}} \mu_{j(3)}^{\text{amp}} \sin(\theta_{j(2)} - \theta_{j(3)}) \\ \mu_{j(3)}^{\text{amp}} \mu_{j(1)}^{\text{amp}} \sin(\theta_{j(3)} - \theta_{j(1)}) \\ \mu_{j(1)}^{\text{amp}} \mu_{j(2)}^{\text{amp}} \sin(\theta_{j(1)} - \theta_{j(2)}) \end{bmatrix} \in \mathbb{R}^3.$$

Then, dipoles with components only in the $l \in [1, 3]$ th axis, i.e., $\mu_{F\perp} = \delta_{il} \in \mathbb{R}^3$, which is Kronecker delta, are obtained by setting $\mu_{F(l)}^{\text{amp}} = 0$ and do not satisfy the above conditions.

B. Power-Optimal Dipole Allocation and Lower Power Bound

The baseline allocation in (8) leads to a decentralized strategy that does not require intersatellite communication; however, these dipole moments are not power-optimal, and this motivated us to derive optimal power-consumption solutions, which are crucial for limited resources. First, we define the overall dipole vector for the $j \in \mathcal{V}_l$ th leader group as

$$m(t) = m(\mu_N^{\text{amp}}, \psi_N, t) = \begin{bmatrix} \sin(\omega_j t) s_N \\ \cos(\omega_j t) c_N \end{bmatrix} \in \mathbb{R}^{6n}$$

where we stack the vectors of the time-varying dipole moments in (1) as $\mu_N^{\text{amp}}, \psi_N, s_N, c_N \in \mathbb{R}^{3n}$. For a given command 6-DoF control f_{cj}, τ_{cj} by an arbitrary controller, the power-optimal dipole solutions m^* satisfy the QCQP problem:

$$\min \int \frac{\|m(\tau)\|^2}{2} \frac{d\tau}{T} \quad \text{s.t.} \quad u_{cj} = u_j^{\text{avg}} \text{ for } j \in [1, n], \quad (10)$$

with an infinite number of solutions [4] and $6n$ equality constraints. For the problem in (10), the associated Lagrangian L with the Lagrange multiplier vector $\lambda \in \mathbb{R}^{6(n-1)}$ is

$$L(m, \lambda) \triangleq \frac{1}{2} m^\top (I_2 \otimes P_\lambda) m - \frac{8\pi}{\mu_0} \lambda^\top [u_{c1}^a; \dots; u_{c(n-1)}^a],$$

where $P_\lambda \triangleq I_{3n} + R_\lambda + R_\lambda^\top$ and $R_\lambda \in \mathbb{R}^{3n \times 3n}$ is the following non-symmetric matrix with $\text{vec}(R_{j \leftarrow k}) \triangleq Q_{j \leftarrow k}^\top \lambda_j$:

$$R_\lambda \triangleq \begin{bmatrix} O_3 & R_{1 \leftarrow 2} & \cdots & R_{1 \leftarrow (n-1)} & R_{1 \leftarrow n} \\ R_{2 \leftarrow 1} & O_3 & \cdots & R_{2 \leftarrow (n-1)} & R_{2 \leftarrow n} \\ \vdots & \vdots & \ddots & \vdots & \vdots \\ R_{(n-1) \leftarrow 1} & R_{(n-1) \leftarrow 2} & \cdots & O_3 & R_{(n-1) \leftarrow n} \\ O_3 & O_3 & \cdots & O_3 & O_3 \end{bmatrix}$$

Note that P_λ is a positive definite matrix; otherwise, there exists an m such that $L(m, \lambda) \rightarrow -\infty$. Then, we obtain the lower bound as $J_{\text{dual}} \leq \frac{1}{2} \|m\|^2$ using the following Lagrange dual problem [15], which is convex and efficiently solvable:

$$\max J_{\text{dual}} = -\frac{8\pi}{\mu_0} \lambda^\top [u_{c1}^a; \dots; u_{c(n-1)}^a] \quad \text{s.t.} \quad P_\lambda \succeq 0. \quad (11)$$

C. Control-Induced Disturbance Reduction via Optimization

Before presenting our learning-based strategy for solving (10) in the next section, we prove that power-optimal dipole allocation also leads to a reduction in time-integrated control-induced disturbances. The rigorous formulation of the magnetic interaction includes $u_{j \leftarrow k}^{\text{avg}}$ in (8) and sinusoidal disturbances $d_{j \leftarrow k}^{2\omega}$ as $u_{j \leftarrow k}(t) = u_{j \leftarrow k}^{\text{avg}} + d_{j \leftarrow k}^{2\omega}$. We can derive the total sinusoidal disturbance from neighbor $d_{j(t)}^{2\omega}$ as

$$d_{j(t)}^{2\omega} = \sum_{k \in \mathcal{N}_j} d_{j \leftarrow k}^{2\omega} = v(t)^\top \begin{bmatrix} d_c \\ d_s \end{bmatrix}, \quad v(t) \triangleq \begin{bmatrix} \cos(2\omega t) \\ \sin(2\omega t) \end{bmatrix} \quad (12)$$

$$\begin{bmatrix} d_c \\ d_s \end{bmatrix} \triangleq \sum_{k \in \mathcal{N}_j} \frac{\mu_0}{8\pi} (I_2 \otimes Q_{j \leftarrow k}) \begin{bmatrix} c_k^b \otimes c_j^b - s_k^b \otimes s_j^b \\ c_k^b \otimes s_j^b + s_k^b \otimes c_j^b \end{bmatrix}.$$

where $\mathcal{N}_j = \{k \mid (j, k) \in \mathcal{E}\}$ is neighbor sets of j th agent. The next lemma states that the solution to the optimization in (10) reduces the upper bound of $\sup_{t \in [0, T]} \|d_{j(t)}^{2\omega}\|$.

Lemma IV.1. $\|m\|^2$ linearly bounds $\sup_{t \in [0, T]} \|d_{j(t)}^{2\omega}\|$.

Proof. We derive the time-supremum $\|d_{j(t)}^{2\omega}\|_2^2$ using (12) as

$$\sup_t \|d_{j(t)}^{2\omega}\|_2^2 = \sup_t v(t)^\top \begin{bmatrix} \|d_c\|^2 & d_c^\top d_s \\ d_c^\top d_s & \|d_s\|^2 \end{bmatrix} v(t)$$

$$\leq \frac{\left\| \begin{bmatrix} d_c \\ d_s \end{bmatrix} \right\|_2^2 + \sqrt{(\|d_c\|_2^2 - \|d_s\|_2^2)^2 + 4(d_c^\top d_s)^2}}{2},$$

where we use $\|v\| = 1$. We define Z_0 and $Z = Z^\top \succ 0$ such that $[c_k^b \otimes c_j^b - s_k^b \otimes s_j^b; c_k^b \otimes s_j^b + s_k^b \otimes c_j^b] = Z_0(m \otimes m)$ and $0 \preceq Z_0^\top (I_2 \otimes Q_{j \leftarrow k})^\top (I_2 \otimes Q_{j \leftarrow k}) Z_0 \preceq (Z \otimes Z)$. Then, $\lambda_{\max}(\cdot) \leq \text{Trace}(\cdot)$ and the Kronecker identity yield

$$\sup_{t \in [0, T]} \|d_{j \leftarrow k}^{2\omega}\|_2^2 \leq \left\| \begin{bmatrix} d_c \\ d_s \end{bmatrix} \right\|_2^2 \leq \left(\frac{\mu_0}{8\pi} m^\top Z m \right)^2.$$

This indicates it is linearly bounded by $\|m\|^2$. \square

Minimizing W_{power} also leads to a reduction in the control-induced disturbance from an uncooperative neighbor using different frequencies, although we omit this proof for simplicity.

V. NEURAL POWER-OPTIMAL DIPOLE ALLOCATION

This subsection presents the learning-based power-optimal dipole calculation model NODA for n agents control. MLP represents the functional mapping from inputs x into outputs such as an $(L+1)$ -layer neural network $\mathcal{F}(x, \theta) = W^{(L+1)} \phi(W^{(L)}(\dots \phi(W^{(1)}x + b^{(1)}) \dots) + b^{(L)}) + b^{(L+1)}$, where the activation function $\phi(\cdot)$ and θ include the weights $\theta_w = W^{(1)}, \dots, W^{(L+1)}$ and bias $\theta_b = b^{(1)}, \dots, b^{(L+1)}$.

A. Minimal Representation of the Dipole Solution

Since we rely on the first-order averaged model in Section II-A, arbitrary $m(\mu_N^{\text{amp}}, \psi_N + \psi_0, t)$ with free parameter ψ_0 and s_j, c_j for all $j, k \in [1, n]$ and $l, m \in \{1, 2, 3\}$,

$$s_{j(t)}(\mu_N^{\text{amp}}, \psi_N, \psi_0) = \mu_{j(t)}^{\text{amp}} \cos(N_c \pi + \psi_0 + \psi_{j(t)})$$

$$c_{j(t)}(\mu_N^{\text{amp}}, \psi_N, \psi_0) = \mu_{j(t)}^{\text{amp}} \sin(N_s \pi + \psi_0 + \psi_{j(t)}) \quad (13)$$

yields the same results as those in (10). Next, we introduce a positive definite matrix variable $\mathfrak{X} \in \mathbb{P}^{3n \times 3n}$ as follows:

$$\mathfrak{X} \triangleq \int_T \frac{\|m(\tau)\|_2^2}{1/2} \frac{d\tau}{T} = \begin{bmatrix} s_N & c_N \\ c_N & s_N \end{bmatrix}^\top,$$

where the final equality denotes $\text{rank}(\mathfrak{X}) \leq 2$. Although this extends $s_N, c_N \in \mathbb{R}^{3n}$ to $\mathfrak{X} \in \mathbb{P}^{3n \times 3n}$, a vector $\mathbf{x}(\mathfrak{X}) \in \mathbb{R}^{9n}$

$$\mathbf{x}(\mathfrak{X}) = [\text{Diag}(\mathfrak{X}); \mathfrak{X}_{(:,1)}; \mathfrak{X}_{(:,2)}] \quad (14)$$

recovers $3n$ -dimensional information by reconstructing the trigonometric terms of each phase.

Lemma V.1 (Reconstructing Phase ψ from \mathfrak{X}). For a given matrix $\mathfrak{X} \in \mathbb{R}^{3n \times 3n}$, we can derive $\mu_N^{\text{amp}} \in \mathbb{R}^{3n}$ and define the phase difference matrix $\text{COS}_{\mathfrak{X}} \in \mathbb{R}^{3n \times 3n}$ as

$$\mu_N^{\text{amp}} = \sqrt{\text{Diag}(\mathfrak{X})}, \quad \text{COS}_{\mathfrak{X}} \triangleq \mathfrak{X} \oslash (\mu_N^{\text{amp}} \mu_N^{\text{amp}\top}), \quad (15)$$

where \oslash denotes element-wise (Hadamard) division. Then,

$$\psi_{1(1)} \triangleq 0, \quad c_{N0} \triangleq c_N(\mu_N^{\text{amp}}, \psi_N, 0) = \mu_N^{\text{amp}} \otimes \text{COS}_{\mathfrak{X}(:,1)}$$

$$s_{N0} \triangleq s_N(\mu_N^{\text{amp}}, \psi_N, 0) = \mu_N^{\text{amp}} \otimes (\text{sign}(\sin \psi_2) \sin \psi_N), \quad (16)$$

where \otimes denotes the element-wise (Hadamard) product and

$$\sin \psi_x \triangleq \frac{\text{COS}_{\mathfrak{X}(x,2)} - \text{COS}_{\mathfrak{X}(x,1)} \text{COS}_{\mathfrak{X}(2,1)}}{\sqrt{1 - \text{COS}_{\mathfrak{X}(2,1)}^2}}. \quad (17)$$

Proof. For readability, we index the $3n$ components using a single index $x, y \in \{1, \dots, 3n\}$ corresponding to $(j, l), (k, m)$:

$$\psi_x \triangleq \psi_{j(l)}, \quad \psi_y \triangleq \psi_{k(m)}, \quad \mathfrak{X}_{(x,y)} \triangleq \mathfrak{X}_{(3(j-1)+l, 3(k-1)+m)}.$$

Note that \mathfrak{X} does not explicitly contain the phases themselves but only their differences because

$$\mathfrak{X}_{(x,y)} = \mu_x^{\text{amp}} \mu_y^{\text{amp}} \cos(\psi_x - \psi_y) \quad (18)$$

holds for all $x, y \in [1, 3n]$. Then, we can derive $\mu_N^{\text{amp}} \in \mathbb{R}^{3n}$ and define the phase-difference information matrix $\text{COS}_{\mathfrak{X}} \in \mathbb{R}^{3n \times 3n}$ in (15). The definition in (13) allows us to assume $\psi_1 \triangleq 0$ and $\text{sign}(\sin \psi_2) \triangleq 1$ without loss of generality. The given $\text{COS}_{\mathfrak{X}}$ satisfies $\text{COS}_{\mathfrak{X}(x,y)} = \cos(\psi_x - \psi_y) = \cos \psi_x \cos \psi_y + \sin \psi_x \sin \psi_y$ based on (18). Subsequently, applying $y = 1$ yields $\cos \psi_x = \text{COS}_{\mathfrak{X}(x,1)}$, and this recovers c_N in (16). Moreover, (18) yields $\text{COS}_{\mathfrak{X}(x,2)} = \cos(\psi_x - \psi_2) = \cos \psi_x \cos \psi_2 + \sin \psi_x \sin \psi_2 = \text{COS}_{\mathfrak{X}(x,1)} \text{COS}_{\mathfrak{X}(2,1)} + \sin \psi_x \sqrt{1 - \text{COS}_{\mathfrak{X}(2,1)}^2}$. Since we have $\cos \psi_2 = \text{COS}_{\mathfrak{X}(2,1)}$, applying $\sin \psi_2 = \sqrt{1 - \cos^2 \psi_2}$ obtains $\sin \psi_x$ in (17). To satisfy $\text{sign}(\sin \psi_2) \triangleq 1$, we define s_N in (16). \square

B. Continuous Power-Optimal Dipole Solutions

We construct a continuous family of locally optimal solutions for the power-optimal allocation using sequential convex programming. This ensures smooth transitions between neighboring optimal configurations and is used to build the MLPs, as described in the next subsection. We consider an input $u^a = [u_1^a; \dots; u_n^a] \in \mathbb{R}^{6n}$ for n agents where

$u_j^a = \frac{\mu_0}{8\pi} \sum_{k \neq j} u_{j \leftarrow k}^a$ by (8). Then, the optimization problem for the power-optimal dipole solution of n agents is

$$\begin{aligned} \min J(m) &= \frac{1}{2} m^\top W m = \frac{1}{2} (s_N^\top W s_N + c_N^\top W c_N) \\ \text{s.t.} \quad &\begin{cases} \forall i \in [1, 6], j \in [1, n-1], \\ \frac{u_{j(i)}^a}{\mu_0/8\pi} = \sum_{k \neq j} Q_{j \leftarrow k(i,:)}^a (s_k^a \otimes s_j^a + c_k^a \otimes c_j^a) \end{cases}, \quad (19) \end{aligned}$$

where the weight matrix is W . Note that the u_j^a are divided by $\mu_0/8\pi = 5e^{-8}$ to avoid excessive trial-and-error calculations. We define $Q_{j \leftarrow k[i]} \in \mathbb{R}^{3 \times 3}$ and $Q_{j[i]} \in \mathbb{R}^{3 \times 3n}$ that satisfy

$$\text{vec}(Q_{j \leftarrow k[i]}) = Q_{j \leftarrow k(i,:)}^\top, \quad Q_{j[i]} \triangleq [Q_{j \leftarrow 1[i]}, \dots, Q_{j \leftarrow n[i]}],$$

Applying \mathfrak{X} in Section V-A and Roth's column lemma derives the trace constraints for $i \in [1, 6]$ th component of u_j^a in (19):

$$\begin{aligned} \frac{u_{j(i)}^a}{\mu_0/8\pi} &= \text{tr} \left[s_j^a \sum_{k \neq j} (Q_{j \leftarrow k[i]} s_k^a)^\top + c_j^a \sum_{k \neq j} (Q_{j \leftarrow k[i]} c_k^a)^\top \right] \\ &= \text{tr} \left[K_j \left(s_N^a (\hat{K}_j s_N^a)^\top + c_N^a (\hat{K}_j c_N^a)^\top \right) (Q_{j[i]} \hat{K}_j^\top)^\top \right] \\ &= \text{tr} [\mathfrak{X} \mathcal{R}_{j[i]}], \quad \mathcal{R}_{j[i]} \triangleq \hat{K}_j^\top \hat{K}_j Q_{j[i]}^\top K_j \in \mathbb{R}^{3n \times 3n} \end{aligned}$$

where $K_j \in \mathbb{R}^{3 \times 3n}$ and $\hat{K}_j \in \mathbb{R}^{(3n-3) \times 3n}$ are

$$\begin{aligned} K_j &= \begin{bmatrix} O_{3 \times 3(j-1)} & I_3 & O_{3 \times 3(n-j)} \\ I_{3(j-1)} & O_{3(j-1) \times 3} & O_{3(j-1) \times 3(n-j)} \\ O_{3(n-j) \times 3(j-1)} & O_{3(n-j) \times 3} & I_{3(n-j)} \end{bmatrix} \\ \hat{K}_j &= \begin{bmatrix} I_{3(j-1)} & O_{3(j-1) \times 3} & O_{3(j-1) \times 3(n-j)} \\ O_{3(n-j) \times 3(j-1)} & O_{3(n-j) \times 3} & I_{3(n-j)} \end{bmatrix}. \end{aligned}$$

We convexify the primal problem in (19) by the standard (Shor) semidefinite program relaxation [15] to derive the unique \mathfrak{X}^* of the power-optimal solutions as follows:

$$\begin{aligned} \text{ODA}_n^{(0)} : \mathfrak{X}_0^* &= \arg \min_{\mathfrak{X} \in \mathbb{S}^{3n \times 3n}} \text{trace}(W\mathfrak{X}) \\ \text{s.t.} \quad \frac{u_{j(i)}^a}{\mu_0/8\pi} &= \text{tr} [\mathfrak{X}_0 \mathcal{R}_{j[i]}], \quad \forall i \in [1, 6], \quad \forall j \in [1, n-1] \end{aligned} \quad (20)$$

As \mathfrak{X}_0^* does not necessarily satisfy the rank conditions $\text{rank}(\mathfrak{X}_0^*) \leq 2$ as mentioned in Section V-A, we reduce its rank using rank-constrained optimization [16]. We solve the sequential convex programming problem for iterations $k > 0$:

$$\begin{aligned} \text{ODA}_n^{(k)} : \mathfrak{X}_k^* &= \arg \min_{\mathfrak{X}_k \in \mathbb{P}^{3n \times 3n}, e_k > 0} \text{trace}(W\mathfrak{X}_k) + w_k e_k \\ \text{s.t.} \quad \frac{u_{j(i)}^a}{\mu_0/8\pi} &= \text{tr} [\mathfrak{X}_k \mathcal{R}_{j[i]}], \quad \forall i \in [1, 6], \quad \forall j \in [1, n-1] \\ V_{k-1}^* \mathfrak{X}_k V_{k-1}^* &\preceq e_k I_{3n-2}, \quad e_k \leq e_{k-1}^*, \end{aligned} \quad (21)$$

where $V_{k-1}^* \in \mathbb{R}^{3n \times (3n-2)}$ denotes the orthonormal eigenvectors of \mathfrak{X}_{k-1}^* associated with its $(3n-2)$ smallest eigenvalues. For matrices \mathfrak{X}_k^* that have converged after k iterations, Lemma V.1 converts \mathfrak{X}_k^* into optimal dipole solutions $m_N^* \in \mathbb{R}^{6N}$. Our trials declared convergence when the third-smallest eigenvalue fell below a certain threshold and stabilized.

Algorithm 2 Convex optimization-based power-optimal dipole allocation for 6-DoF MTQ control of n -agents.

- 1: **Inputs:** position/command $\setminus_N \in \mathbb{R}^{3n}, \cong_N \in \mathbb{R}^{6n}$
- 2: **Outputs:** $\mu_j^{a*}(t) \in \mathbb{R}^3, j \in [1, n]$
- 3: Define the base frame $\{\mathcal{A}\}$ and derive r_j^a and u_j^a
- 4: Solve dual problem in (11) for J_{dual}
- 5: Solve ODA $_n$ in (20) and (21) for \mathfrak{X}^* and extract \mathbf{x}
- 6: Recover s_{N0}^*, c_{N0}^* from \mathfrak{X}^* by Lemma V.1
- 7: Choose ψ_0 , e.g., Remark 4 and derive $\mu_j^{a*}(t)$ in (13)

C. Learning-based Dipole Allocation Model

This subsection summarizes the offline training method of the learning-based optimal dipole model NODA. To mitigate the curse of dimensionality for training, we chose the base frame as the line-of-sight frame $\{\mathcal{LOS}_{j \leftarrow k}\}$ of an arbitrary k th follower. The formulation in (8) reduces $[r_{j \leftarrow k}^a; u_j^a] \in \mathbb{R}^9$ to $[d_{j \leftarrow k}; f_{j(1,2)}^a; \tau_j^a] \in \mathbb{R}^6$. Then, the NODA model takes $9(N-1)-3$ dimensional agent states of the specific $j \in \mathcal{V}_l$ th leader agents and yields the optimal \mathbf{x}^* in (14) as follows:

$$\mathbf{x}^* = \mathfrak{M}([r^{l_{j \leftarrow k}}, f^{l_{j \leftarrow k}}, \tau^{l_{j \leftarrow k}}], \boldsymbol{\theta}) \quad \text{s.t.} \quad (19),$$

to derive dipole solutions s_{N0}^*, c_{N0}^* via Lemma V.1. Although this NODA model \mathfrak{M} is naturally controller-invariant, limiting the input norm via gain-tuning and guidance strategy reduces the sample region of f and τ to deal with the curse-of-dimensionality problem. Moreover, the distance-dependent magnetic field property naturally restricts r to a small region.

Remark 3. *NODA is attitude-invariant when the far-field model is used. An exact model [7] includes the attitude information, thereby increasing the input dimensionality; otherwise, we decouple and compensate through controller design [5].*

Remark 4. *Discontinuously switching $m_{(t_-)}$ into $m_{(t_+)}$ at time t induces an impulse input that may excite disturbances in the high-frequency band. The free parameter ψ_0 can address this problem such that $\psi_0^* = \arg \min \|m_{(t_-)} - m_{(t_+, \psi_0)}\|$.*

VI. VALIDATION OF NODA MODEL

We validated our learning-based dipole allocation algorithm and multileader-based decentralization through numerical simulations and experiments on formation and attitude control. Our control goal was to achieve a regular triangle with a distance r_d and their attitudes aligned with the others.

A. Two-Dimensional Micro-Gravity Experiment Setup

We conduct numerical simulations replicating the ground-based environment [5] in Fig 2d as shown in Fig. 2a. This subsection briefly overviews the setup; a full description can be found in [5]. The testbed consists of a two-axis MTQ capable of generating horizontal-plane magnetic fields with one coil incorporating an iron core. The microcomputers achieve time synchronization via the GPS pulse-per-second signal with 0.1 ms accuracy. Then, we set the candidates of ω_j as $\omega_j = 8\pi \times \{1:5\}$ rad/s for the time-averaged model. As illustrated in Fig. 2d, MTQ assemblies were mounted on a linear air

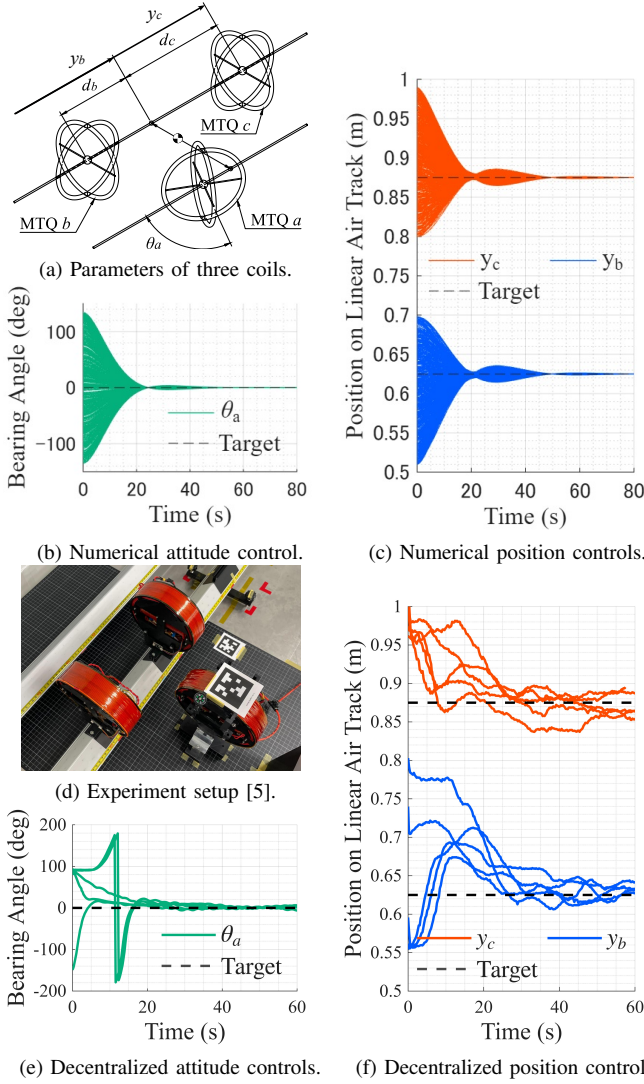


Fig. 2. Numerical simulation results in Figs 2b and 2c and experimental results using the linear air track and single-axis air bearing [5] in Figs 2e and 2f applied the controller and decentralized allocation in subsection VI-B.

track and a single-axis air bearing. We partially justified their mechanical constraints the following assumptions.

Assumption 1. *Forces and torques are parallel to the movable directions of the linear air track and air bearing, respectively.*

The base frame was defined as follows: the y -axis was along the linear track, and the z -axis was normal to the table. The origin was set such that the y axis penetrated the geometric center of MTQs b & c , and the x axis completed a right-handed orthogonal frame. The positions of the MTQs were defined as $p_a \triangleq [\frac{\sqrt{3}}{2}r_d; \frac{L_{air}}{2}; 0]$ and $p_{b,c} \triangleq [0; y_{b,c}; 0]$ where $y_b < y_c$.

B. Kinematics Controller and Dipole Allocation Design

We designed a formation and attitude controller using Theorem II.1 and the multileader-based control introduced in Section III. For a decentralized allocation, we separated the three coils into three groups, and each pair of MTQs, a - b , b -

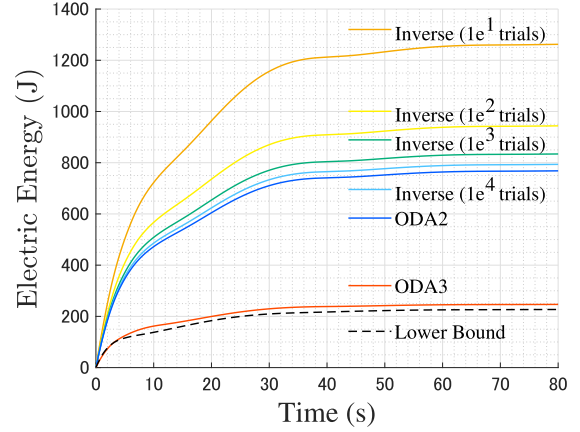


Fig. 3. Numerical simulation results of energy consumption of the decentralized and centralized allocations with the lower bound given in (11).

c , and c - a , is controlled in a decentralized manner via different frequencies. Their adjacency matrices are

$$A_1 = \begin{bmatrix} 0 & 1 & 0 \\ 1 & 0 & 0 \\ 0 & 0 & 0 \end{bmatrix}, \quad A_2 = \begin{bmatrix} 0 & 0 & 0 \\ 0 & 0 & 1 \\ 0 & 1 & 0 \end{bmatrix}, \quad A_3 = \begin{bmatrix} 0 & 0 & 1 \\ 0 & 0 & 0 \\ 1 & 0 & 0 \end{bmatrix}.$$

and their Laplacian matrix $L_i \triangleq \text{Diag}(A_i \mathbf{1}) - A_i$ with the vector of all ones $\mathbf{1}$ derives auxiliary commands $u_{c[i]}^a \in \mathbb{R}^{24}$:

$$u_{c[i]}^a = \begin{bmatrix} f_c^a \\ \tau_c^a \\ \dot{h}_{c1}^a \end{bmatrix} = -(L_i \otimes I_9)(K_p(x - x_d) + K_d(\dot{x} - \dot{x}_d)),$$

which includes $x = [p_N; \theta_N; \xi_1^{b1}; \xi_2^{b2}]$. Theorem II.1 derives the commands for decentralized and centralized allocation:

$$u_{c[i]}^a = B_{(3,2)}^{-1} M_{(3,2)} S_{(2,2)[i]} u_{c[i]}^a, \quad u_c^a = \sum_{i \in \mathcal{V}_i} u_{c[i]}^a$$

where $S_{(2,2)[i]}$ is the associated tangent space of angular momentum conservation for each pair in subsection II-B.

We experimentally verified this decentralized allocation for three-coil control. Each pair converts $u_{c[i]}^a$ to the dipoles based on (9) and drive the currents at $\omega_j = 8\pi \times \{1, 2, 3\}$ rad/s. The experimental result in Fig. 2 shows that their states stabilize around the desired ones under the microgravity of the linear air track. This partially highlights the scalability extension of the multileader-based control introduced in Section III.

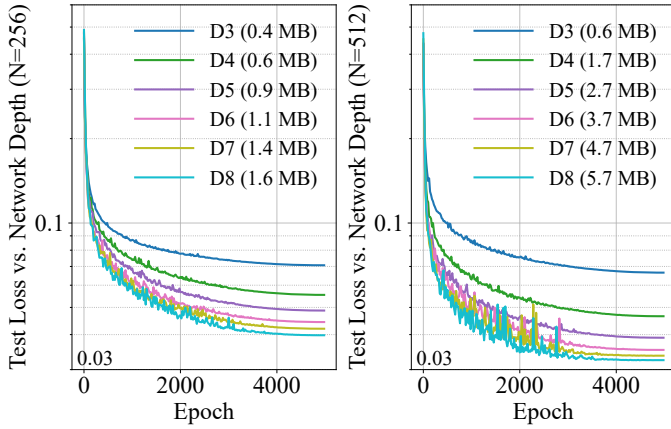
C. Numerical Optimality Comparison of ODA and Baseline

We numerically compare the power optimality of ODA_n in (20) and (21) with the baseline in (9) for the three coils formation and attitude control. We conducted 500 numerical simulations using the command inputs u_c in subsection VI-B. Figures 2b and 2c show the obtained time-series data, and we convert them to associated dipole via three dipole allocations: the centralized allocation ODA_3 and a two decentralized allocations (inverse method in Algorithm 1 with $1e^4$ trials and ODA_2). We define a power index as W_{power} :

$$W_{\text{power}} \triangleq R \int_T c_i^2(\tau) \frac{d\tau}{T} = R \frac{\|\mu_N^{\text{amp}}\|^2}{2\gamma_{\mu/c}^2} \geq R \frac{J_{\text{dual}}}{\gamma_{\mu/c}^2}$$

TABLE I
NUMERICAL PERFORMANCE COMPARISONS: POWER CONSUMPTION AND CONTROL-INDUCED DISTURBANCE REDUCTION.

Allocations	Inverse $\times 1e^4$ trials	ODA ₂	ODA ₃
Command	$u_c = B_{(3,2)}^{-1} M_{(3,2)} S_{(3,2)} u_a$		
Grouping	Decentralized	Centralized	
Power (J)	790-1250	760	250
Δf (%)	5.4	5.15	0.40
$\Delta \tau$ (%)	5.1	5.0	0.53



(a) Test loss for network of $N = 256$. (b) Test loss for network of $N = 512$.
Fig. 4. The trade-off between model size and performance of learning.

where $R \approx 2.1\Omega$ is the coil resistor [5], $\gamma_{\mu/c} \approx 2.1m^2$ is the coil design ratio [5], and the lower bound J_{dual} in (11). Note that we memorize minimum values of the inverse method for each trials. We also derived the indexes $\Delta\{f, \tau\} \in \mathbb{R}$ to investigate time-integrated control-induced disturbances:

$$\Delta\{f, \tau\} \triangleq \sup_k \sup_{j \in \mathcal{V}} \frac{\|\{f, \tau\}_{jc} - \sup_{t \in [t_{[k]}, t_{[k]}+T]} \{f, \tau\}_{j(t)}\|_2}{\|\{f, \tau\}_{jc}\|_2}.$$

The calculation results in Fig. 3 and Table I show the integration of W_{power} and $\Delta\{f, \tau\}$. The inverse approach showed large variations in energy consumption across $1e^4$ trials and converged to a performance close to that of the ODA₂ result. Notably, the centralized ODA₃ achieved significantly better power efficiency, requiring only approximately one-third to one-fifth of the power consumption compared to ODA₂ and inverse allocation with 10 trials. This arises from magnetic field anisotropy, implying that certain directions are more effective for generating control inputs within a given power limit. In the two-dimensional setup, the three satellites cooperatively compensate for this anisotropy, thereby enabling the derivation of a more power-optimal current solution. We also confirm the reduction of $\Delta\{f, \tau\}$ by the power optimization in Table I as proved in Section IV-C, which reduces steady-state errors.

D. Offline Supervised Learning for NODA Construction

This subsection presents the numerical validation of the trained NODA model for Ten MTQs and the scalability extension by time-integrated control. We first train NODA \mathfrak{M} for a three-coil formation and attitude control based on

Section V. Assumption 1 indicates f^a has only y components and τ^b has only z components. Subsequently, along with linear and angular momentum conservation, we reduced the input data for our experiment to the following six variables: $\chi = [y_1; y_2; f_{1y}^a; f_{2y}^a; \tau_{1z}^b; \tau_{3z}^b] \in \mathbb{R}^6$ and the 15 dimensional label data x , after removing redundant and zero components. This study collected 3.5 million training samples using Algorithm 2 for the regions shown in Figs. 2b and 2c. Our model $\mathfrak{M}(\chi, \theta)$ is composed of six ($\triangleq D-1$) hidden layers with 256 ($\triangleq N$) neurons and one hidden layer with 128 neurons, based on the trade-off between model size and test loss in Fig. 4. The activation function is an element-wise Leaky Rectified Linear Unit function. The batch sizes were 131,072 and the learning rate followed a cosine-annealing schedule, decreasing from 10^{-3} to 10^{-6} during $5e^3$ epoch. The training used a smooth L1-loss function that converged to a training loss of $2.66e^{-2}$ and a test loss of $3.59e^{-2}$. This result shows that the solutions derived in Algorithm 2 successfully capture the features of an infinite number of optimal solutions to the non-convex problem in (10).

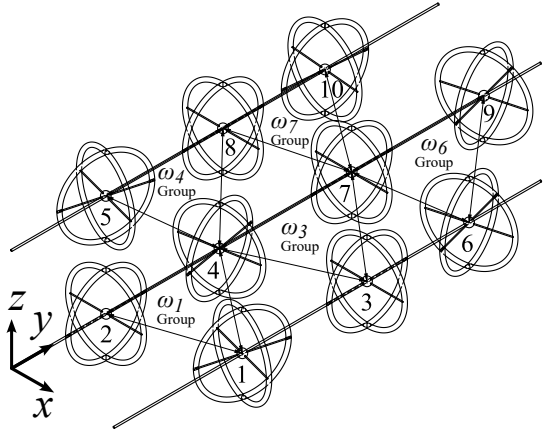
E. Learning-based Power-Optimal 10 MTQs Control

We apply the trained NODA model to Ten MTQs control and numerically demonstrate scalability via time-integrated control. We assume Ten MTQs are divided into five groups managed by leaders $[1, 3, 4, 6, 7] \in \mathcal{V}_l$ using AC frequencies $\omega_{1,3,4,6,7} = 8\pi \times \{1:5\}$ rad/s as shown in Fig. 5a. Each leader decentrally converts local state and control vectors to the power-optimal dipoles by NODA model $\mathfrak{M}(\chi, \theta)$ and Lemma V.1. For five cases using different initial conditions, their formation and attitude converge the desired states defined in subsection VI-B. We plot the control results of a total of 15 edges, the norm of the relative position, with the same case indicated by the same color in Fig. 5b. The power consumption was dramatically reduced one-third to one-ten for both the initial damping phase and steady-state control, as reported in Fig. 5c. These results are consistent with those reported in subsection VI-C.

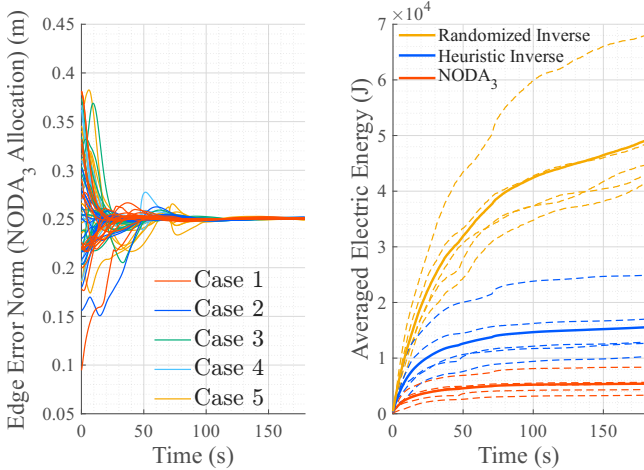
The figures 6 present the duality gap [15] of ODA₃ and the allocation time comparison obtained from time-series data in the 10-agent control. As shown in Fig. 6a, the duality gap between ODA₃ and its dual problem in (11) is nearly zero, and ODA₃ does not lose global optimality for our planar swarm control scenario. General verification is left for future work. As illustrated in Fig. 6b, the proposed NODA model reduces the computation time by about 1/50,000, comparable to the inverse approach. These results demonstrate that the proposed learning-based framework successfully achieves both optimality and computational efficiency. Combining our multileader-based control with NODA_n achieves power-optimal current allocation for an arbitrary number of agents.

VII. CONCLUSION

This paper introduces a learning-based current calculation framework for power-optimal control of magnetically actuated systems. Because power-efficient dipole computation incurs

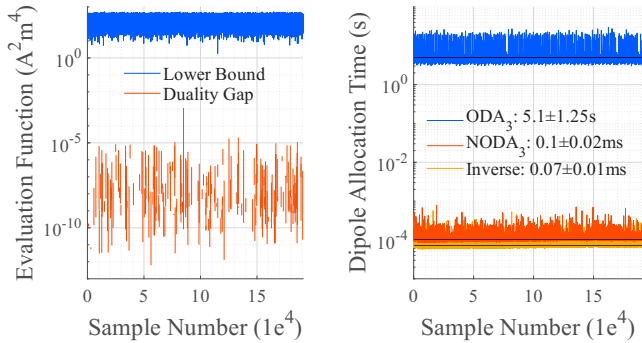


(a) Ten MTQs belong to five groups with five AC frequencies.



(b) Formation control command results. (c) Energy consumption results.

Fig. 5. Multileader-based decentralized control overview and numerical simulation results for 10 MTQs control using trained NODA.

(a) Duality gap comparison of ODA₃. (b) Allocation time comparison.Fig. 6. Duality gap of ODA₃ problem and the allocation time comparison for 10 MTQs control in subsection VI-E. All computations were performed in MATLAB R2025a on a workstation with an AMD Ryzen Threadripper 7980X and 64 GB RAM (Windows 11 Pro, 64-bit).

high computational costs, we present an optimal solution calculation using sequential convex optimization and approximate it with a data-driven model, NODA. To accommodate large robot groups, a systematic decoupling architecture is employed to partition the agents into smaller units. Experimental and Numerical results show the effectiveness of our decentraliza-

tion strategy, and the trained model accurately reproduces the targeted magnetic interactions while reducing power consumption, control-induced disturbances, and computation time. The proposed framework offers a practical solution for generating current commands in resource-constrained robotic systems.

ACKNOWLEDGMENTS

This work was supported by the JST's Next-Generation Challenging Research Program JPMJSP2106 and the JAXA Space Strategy Fund GRANT Number (JPJXSSF24MS09003), Japan. The authors would like to thank Associate Prof. Yoichi Tomioka at the University of Aizu and Hayate Tajima at The University of Tokyo for technical discussions, and Atsuki Ochi at Interstellar Technologies Inc. for assistance with controller gain tuning.

REFERENCES

- [1] Q. Ze, S. Wu, J. Nishikawa, J. Dai, Y. Sun, S. Leanza, C. Zemelka, L. S. Novelino, G. H. Paulino, and R. R. Zhao, "Soft robotic origami crawler," *Science Advances*, vol. 8, no. 13, p. eabm7834, 2022.
- [2] S.-I. Sakai, Y. Fukushima, and H. Saito, "Design and on-orbit evaluation of magnetic attitude control system for the "reimei" microsatellite," in *10th IEEE International Workshop on Advanced Motion Control*. IEEE, 2008, pp. 584–589.
- [3] T. Shibata, H. E. Söken, and S.-i. Sakai, "Relative position estimation using modulated magnetic field for close proximity formation flight," *Aerospace Science and Technology*, vol. 155, p. 109597, 2024.
- [4] Y. Takahashi, H. Sakamoto, and S.-i. Sakai, "Kinematics control of electromagnetic formation flight using angular-momentum conservation constraint," *Journal of Guidance, Control, and Dynamics*, vol. 45, no. 2, pp. 280–295, 2022.
- [5] Y. Takahashi, A. Ochi, Y. Tomioka, and S.-I. Sakai, "Noda-mmh: Certified learning-aided nonlinear control for magnetically-actuated swarm experiment toward on-orbit proof," in *International Conference on Space Robotics 2025*. IEEE, 2025.
- [6] J. L. Ramirez Riberos, "New decentralized algorithms for spacecraft formation control based on a cyclic approach," Ph.D. dissertation, Massachusetts Institute of Technology, 2010.
- [7] Y. Takahashi, H. Tajima, and S.-i. Sakai, "Certified coil geometry learning for short-range magnetic actuation and spacecraft docking application," *arXiv preprint*, 2025.
- [8] S. Shim, Y. Takahashi, N. Usami, M. Kubota, and S.-i. Sakai, "Feasibility analysis of distributed space antennas using electromagnetic formation flight," in *2025 IEEE Aerospace Conference*, 2025, pp. 1–18.
- [9] Y. Takahashi, S. Shim, and S.-i. Sakai, "Distance-based relative orbital transition for palm-sized satellite swarm with guaranteed escape-avoidance," in *AIAA Scitech 2025 Forum*, 2025, p. 2068.
- [10] S. A. Schweighart, "Electromagnetic formation flight dipole solution planning," Ph.D. dissertation, Massachusetts Institute of Technology, 2005. [Online]. Available: <http://hdl.handle.net/1721.1/32464>
- [11] E. Fabacher, S. Lizy-Destrez, D. Alazard, F. Ankersen, and A. Profizi, "Guidance of magnetic space tug," *Advances in Space Research*, vol. 60, no. 1, pp. 14–27, 2017.
- [12] J. J. Abbott, J. B. Brink, and B. Osting, "Computing minimum-power dipole solutions for interdipole forces using nonlinear constrained optimization with application to electromagnetic formation flight," *IEEE Robotics and Automation Letters*, vol. 2, no. 2, pp. 1008–1014, 2017.
- [13] Z. Abbasi, J. B. Hoagg, and T. M. Seigler, "Decentralized electromagnetic formation flight using alternating magnetic field forces," *IEEE Transactions on Control Systems Technology*, vol. 30, no. 6, pp. 2480–2489, 2022.
- [14] Y. Takahashi, S. Seang, S. Yusuke, Y. Hideki, I. Masaru, I. Norit-suna, M. Sumio, S. Shin-Ichiro, and I. Takahiro, "Experimental study of magnetically-actuated satellite swarm: Controllability extension via time-integrated control with geometry learning," in *SMC-IT/SCC 2025 Space Robotics Workshop*. IEEE, 2025.
- [15] S. P. Boyd and L. Vandenberghe, *Convex Optimization*. Cambridge University Press, 2004.
- [16] C. Sun and R. Dai, "Rank-constrained optimization and its applications," *Automatica*, vol. 82, pp. 128–136, 2017.